# Design of Prestressed Skin–Flange Assembly

KAREL MATOUŠ AND GEORGE J. DVORAK*

*Department of Mechanical Aerospace and Nuclear Engineering
Rensselaer Polytechnic Institute
110 8th Street, Troy, NY 12180*

**ABSTRACT:** A prestressing procedure for reduction of adhesive peel and shear stresses at the leading edge of a skin–flange assembly is analyzed for tensile and bending loads applied to the skin. Both an analytical solution based on the Green's functions and a finite element solution are presented for specific examples, together with design diagrams. Substantial shear and peel stress reductions are obtained with the proposed procedure.

**KEY WORDS:** skin–flange assembly, adhesive bonding, prestress procedure, design diagram.

## INTRODUCTION

**M**ANY COMPOSITE STRUCTURES contain skin–flange assemblies that provide attachment and support for stringers and other parts of the structure. Adhesive joints which are typically used in such applications are exposed to large stress concentrations at the leading edges of the bondline and the adjacent end of the flange. Joint failures often originate at these locations, as shown in numerous experiments by Kevin O'Brien's group at NASA-Langley [1–3].

The present work shows that the stress concentrations contributing to such joint failures can be reduced or eliminated altogether by certain prestress forces applied to the skin–flange assembly prior to and removed after adhesive cure. Prestress application can be accomplished by simple fixtures, as described in the next section. The residual stress distributions

---

*Author to whom correspondence should be addressed. E-mail: dvorak@rpi.edu

and their superposition with the fields induced by mechanical loading are analyzed both by the Green's functions-based analysis (GFA) proposed by Gao et al., [4,5] and by the finite element method (FEM). The GFA is augmented here with functions that allow evaluation of the longitudinal normal strain in the adhesive layer.

A specific skin–flange assembly is selected and subjected to prestress followed by adhesive cure, prestress release, and to subsequent mechanical loading by tension and bending applied to the skin. Numerous comparisons of the adhesive stress distributions obtained by the two methods are presented, which show reasonably good agreement, except in those parts of the adhesive layer which experience large changes in local stress gradients. Design diagrams based on elastic adherend and adhesive response are constructed for evaluation of prestress forces that reduce or completely cancel adhesive stress components induced at the leading edges of the bondline by selected skin loads. Several conclusions and extended use of the design diagrams under cyclic loads are discussed.

## PRESTRESSED SKIN–FLANGE ASSEMBLY

A typical geometry of the problem under consideration appears in Figure 1(a), which shows a flange adhesively bonded at one surface of a continuous skin plate. The flange serves to attach a frame or stiffener to the skin, say of a bonded fuselage panel. Complex in-plane and out-of-plane loading of the panel is usually present in service, however, the load components that contribute most to local failure of the adhesive bond at flange ends are in-plane tension and transverse bending stresses, applied to the skin. These loads generate shear and peel stress concentrations at the ends (points $D$) of the adhesive layer, making them
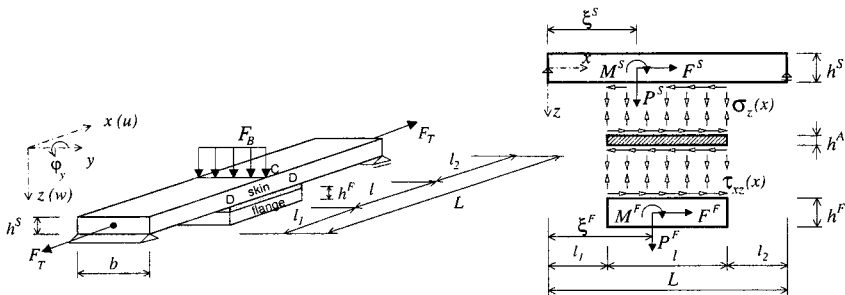


**Figure 1.** (a) Geometry and load of the skin/flange assembly; (b) Free body diagram.
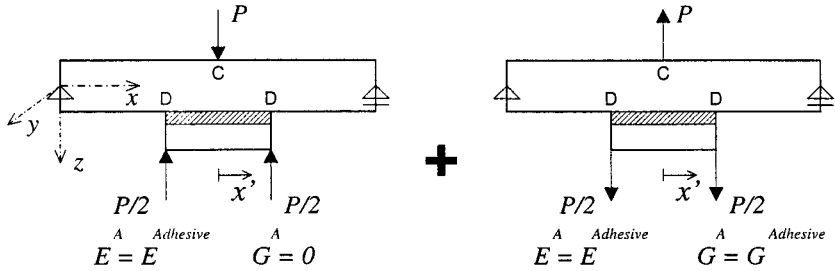
**Figure 2.** Prestress procedure.

preferred sites of adhesive failure or delamination at ply ends in a composite flange.

Our objective is to propose and analyze a controlled prestressing sequence applied during adhesive bonding of the flange, that introduces a favorable residual stress distribution at both ends of the bondline, and thus should enhance the load bearing capacity of the joint. The loading sequence and adhesive property changes applied during the prestressing procedure are illustrated in Figure 2. First, an adhesive layer is applied in the usual way to the skin–flange bondline. While the adhesive ($^A$) is still liquid, the skin is loaded at point $C$ by the prestress line force $P$ distributed uniformly across the width $b$ of the assembly. The assembly is supported at the end points $D$ of the flange; in practice the forces $P/2$ would be applied to small pads, preferably filled with a sealed liquid to assure uniform local distribution. Under the prestress load, the adhesive in the bondline is assumed to have no resistance to shearing, while being able to transmit the compressive stress distribution between skin and flange. Therefore, the shear and Young's moduli of the liquid adhesive are selected as $G^A = 0$ and $E^A = E^{\text{Adhesive}}$, the value in the cured state. After cure, but prior to release of the prestress force $P$, the $G^A$ is restored to $G^A = G^{\text{Adhesive}}$. A certain part of the bending deflection is recovered, but another part is retained by the residual shear and peel stresses in the adhesive. At the leading edges $D$ of the flange, both the residual adhesive shear and peel stresses have an opposite sign to those caused by the in-plane tension force $F_T$ and/or by the bending force $F_B$, Figure 1a. The residual peel stress in the adhesive is compressive and thus helps in reducing the tensile peel stress caused by each of the two forces.

The present analysis is concerned with evaluation of the stresses caused in the adhesive bondline by applied tensile and bending forces $F_T$ and $F_B$, and also of the residual stresses caused there by release of the prestress force $P$.

Results of the elastic solution are combined in design diagrams which allow selection of the prestress force such that the superimposed applied and residual stresses in the adhesive reach a selected minimum value. Both flange and skin are assumed to be made of the same homogeneous isotropic elastic material, however the technique would allow different moduli be prescribed in flange and skin. The adhesive conforms to the same assumptions, with different elastic moduli.

## GREEN'S FUNCTIONS ANALYSIS
## OF THE SKIN–FLANGE ASSEMBLY

This part of the analysis is based on the set of Green's functions derived in Appendix A, which evaluate the deflection and rotation, caused at any point $0 \leq x \leq l$ of a simply supported beam, by forces and moments applied at a selected point $\xi$; $0 \leq \xi \leq l$. Figure 1(a) shows the geometry and dimensions of the assembly to be analyzed, and Figure 1(b) presents the free body diagrams of the adherents and adhesive. The objective is to evaluate the peel and shear stresses in the adhesive layer due to the loads shown in Figures 1(a) and 1(b). To this end, we first express the generalized displacements (deflection, rotation and longitudinal displacement) caused in the skin ($^S$) by the loads $P^S$, $M^S$, $F^S$.

$$w^S = P^S \Gamma_P^S(x, \xi^S, L) + M^S \Gamma_M^S(x, \xi^S, L) + b^A \int_{l_1}^{l} \sigma_z(\xi) \Gamma_P^S(x, \xi, L) \mathrm{d}\xi$$

$$+ \frac{b^A h^S}{2} \int_{l_1}^{l} \tau_{xz}(\xi) \Gamma_M^S(x, \xi, L) \mathrm{d}\xi$$

$$\varphi_y^S = P^S \tilde{\Gamma}_P^S(x, \xi^S, L) + M^S \tilde{\Gamma}_P^S(x, \xi^S, L) + b^A \int_{l_1}^{l} \sigma_z(\xi) \tilde{\Gamma}_P^S(x, \xi, L) \mathrm{d}\xi$$

$$+ \frac{b^A h^S}{2} \int_{l_1}^{l} \tau_{xz}(\xi) \tilde{\Gamma}_P^S(x, \xi, L) \mathrm{d}\xi$$

$$u_0^S = F^S \Gamma_F^S(x, \xi^S, L) - b^A \int_{l_1}^{l} \tau_{xz}(\xi) \Gamma_F^S(x, \xi^S, L) \mathrm{d}\xi. \tag{1}$$

The bottom beam ($^F$) representing the flange in Figure 1(b) is loaded by the bondline tractions, together with the forces $P^F$, $F^F$ and the moment $M^F$. Using again the Green's functions, the displacement, rotations and

translation can be found in the form,

$$w^F = P^F \Gamma_P^F(x, \xi^F, l) + M^F \Gamma_M^F(x, \xi^F, l) - b^A \int_{l_1}^{l} \sigma_z(\xi) \Gamma_P^F(x, \xi, l) \mathrm{d}\xi$$

$$+ \frac{b^A h^F}{2} \int_{l_1}^{l} \tau_{xz}(\xi) \Gamma_M^F(x, \xi, l) \mathrm{d}\xi + \omega_0 + \omega_1 x$$

$$\varphi_y^F = P^F \tilde{\Gamma}_P^F(x, \xi^F, l) + M^F \tilde{\Gamma}_M^F(x, \xi^F, l) - b^A \int_{l_1}^{l} \sigma_z(\xi) \tilde{\Gamma}_P^F(x, \xi, l) \mathrm{d}\xi$$

$$+ \frac{b^A h^F}{2} \int_{l_1}^{l} \tau_{xz}(\xi) \tilde{\Gamma}_M^F(x, \xi, l) \mathrm{d}\xi + \omega_1$$

$$u_0^F = F^F \Gamma_F^F(x, \xi^F, l) + b^A \int_{l_1}^{l} \tau_{xz}(\xi) \Gamma_F^F(x, \xi, l) \mathrm{d}\xi + \omega_2 \tag{2}$$

where $\omega_0$, $\omega_2$, and $\omega_1$ denote the yet unknown rigid body deflection, translation and rotation. These are found from the equilibrium requirements for the flange ($^F$), given by,

$$-b^A \int_{l_1}^{l} \sigma_z(\xi) \mathrm{d}\xi + P^F = 0$$

$$-b^A \int_{l_1}^{l} \sigma_z(\xi) \xi \mathrm{d}\xi + M^F - F^F \frac{h^F}{2} + P^F \xi^F = 0$$

$$b^A \int_{l_1}^{l} \tau_{xz}(\xi) \mathrm{d}\xi + F^F = 0. \tag{3}$$

Response of the adhesive layer ($^A$) in the $xz$-plane is governed by the constitutive relations,

$$\left\{ \begin{array}{c} \sigma_x(x) \\ \sigma_z(x) \\ \tau_{xz}(x) \end{array} \right\} = \left[ \begin{array}{ccc} \bar{E} & v^A \bar{E} & 0 \\ v^A \bar{E} & \bar{E} & 0 \\ 0 & 0 & G \end{array} \right] \left\{ \begin{array}{c} \varepsilon_x(x) \\ \varepsilon_z(x) \\ \gamma_{xz}(x) \end{array} \right\} \tag{4}$$

where $\bar{E} = E/[1 - (v^A)^2]$ for plane stress $\sigma_y(x) = 0$ and $\bar{E} = E(1 - v^A)/[(1 + v^A)(1 - 2v^A)]$ for plane strain $\varepsilon_y(x) = 0$, which is more appropriate for the present application. Identifying the bondline tractions at point $\xi$ with the stresses in the adhesive layer provides,

$$\sigma_z(x) = \bar{E}^A[v^A \varepsilon_x(x) + \varepsilon_z(x)]$$

$$\tau_{xz}(x) = G^A \gamma_{xz}(x). \tag{5}$$
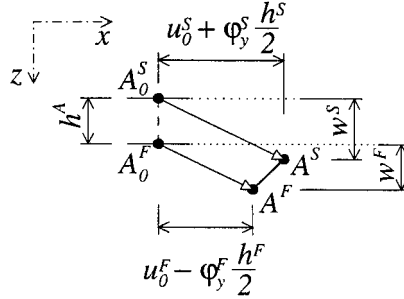
**Figure 3.** *Displacements in the adhesive layer.*

Strains in the adhesive are derived as layer thickness averages, from the relative displacements of the skin and flange, which are shown in Figure 3. The relative displacements are expressed by,

$$A^S - A_0^S = u_0^S + \varphi_y^S \frac{h^S}{2}$$

$$A^F - B_0^S = u_0^F - \varphi_y^F \frac{h^F}{2}$$

$$u_0^A = \frac{(A^S - A_0^S) + (A^F - A_0^F)}{2} \tag{6}$$

so that the average adhesive layer strains become,

$$\varepsilon_x(x) = \frac{\partial u_0^A}{\partial x} = \frac{1}{2}\left[\frac{\partial u_0^S}{\partial x} + \frac{h^S}{2}\frac{\partial \varphi_y^S}{\partial x} + \frac{\partial u_0^F}{\partial x} - \frac{h^F}{2}\frac{\partial \varphi_y^F}{\partial x}\right]$$

$$\varepsilon_z(x) = \frac{w^F - w^S}{h^A}$$

$$\gamma_{xz}(x) = \frac{(A^S - A_0^S) - (A^F - A_0^F)}{h^A} = \frac{u_0^S - u_0^F}{h^A} + \frac{\varphi_y^S h^S + \varphi_y^F h^F}{2h^A}. \tag{7}$$

Substituting from (1) and (2) to (7) and then (5) provides the following system of integral equations for the unknown bondline tractions,

$$\sigma_z(x) + \int_{l_1}^{l} \sigma_z(\xi)[K_1\mathcal{A} + K_2\mathcal{B}]\mathrm{d}\xi + \int_{l_1}^{l}\tau_{xz}(\xi)[K_1\{\mathcal{C}+\mathcal{D}\} + K_2\{\mathcal{E} - \omega_0 - \omega_1 x\}]\mathrm{d}\xi$$

$$= K_1\{\mathcal{I}\mathcal{J}\mathcal{K}\} + K_2\{\mathcal{L}\mathcal{M}\}$$

$$\tau_{xz}(x) + \int_{l_1}^{l}\sigma_z(\xi)[K_3\mathcal{F}]\mathrm{d}\xi + \int_{l_1}^{l}\tau_{xz}(\xi)\left[K_3\left\{\mathcal{G} - \mathcal{H} - \omega_1\frac{h^F}{2} + \omega_2\right\}\right]\mathrm{d}\xi$$

$$= K_3\{\mathcal{N}\mathcal{O}\mathcal{P}\} \tag{8}$$

where

$$K_1 = \frac{\bar{E}^A v^A}{2} \quad K_2 = \frac{\bar{E}^A}{h^A} \quad K_3 = \frac{G^A}{h^A} \tag{9}$$

and the terms $\mathcal{A}, \mathcal{B}, \mathcal{C}, \mathcal{D}, \mathcal{E}, \mathcal{F}, \mathcal{G}, \mathcal{H}$ contain Green's functions,

$$
\begin{aligned}
\mathcal{A} &= -\frac{h^S}{2}\frac{\partial}{\partial x}\tilde{\Gamma}_P^S(x, \xi, L) - \frac{h^F}{2}\frac{\partial}{\partial x}\tilde{\Gamma}_P^F(x, \xi, l) \\
\mathcal{B} &= \Gamma_P^S(x, \xi, L) + \Gamma_P^F(x, \xi, l) \\
\mathcal{C} &= \frac{\partial}{\partial x}\Gamma_F^S(x, \xi, L) - \frac{\partial}{\partial x}\Gamma_F^F(x, \xi, l) \\
\mathcal{D} &= -\frac{(h^S)^2}{4}\frac{\partial}{\partial x}\tilde{\Gamma}_M^S(x, \xi, L) + \frac{(h^F)^2}{4}\frac{\partial}{\partial x}\tilde{\Gamma}_M^F(x, \xi, l) \\
\mathcal{E} &= \frac{h^S}{2}\Gamma_M^S(x, \xi, L) - \frac{h^F}{2}\Gamma_M^F(x, \xi, l) \\
\mathcal{F} &= -\frac{h^S}{2}\tilde{\Gamma}_P^S(x, \xi, L) + \frac{h^F}{2}\tilde{\Gamma}_P^F(x, \xi, l) \\
\mathcal{G} &= \Gamma_F^S(x, \xi, L) + \Gamma_F^F(x, \xi, l) \\
\mathcal{H} &= \frac{(h^S)^2}{4}\tilde{\Gamma}_M^S(x, \xi, L) + \frac{(h^F)^2}{4}\tilde{\Gamma}_M^F(x, \xi, l).
\end{aligned}
\tag{10}
$$

The load-related terms are,

$$
\begin{aligned}
\mathcal{I} &= F^S\frac{\partial}{\partial x}\Gamma_F^S(x, \xi, \xi^S, L) + F^F\frac{\partial}{\partial x}\Gamma_F^F(x, \xi^F, l) \\
\mathcal{J} &= \frac{h^S P^S}{2}\frac{\partial}{\partial x}\tilde{\Gamma}_P^S(x, \xi^S, L) - \frac{h^F P^F}{2}\frac{\partial}{\partial x}\tilde{\Gamma}_P^F(x, \xi^F, l) \\
\mathcal{L} &= -P^S\Gamma_P^S(x, \xi^S, L) + P^F\Gamma_P^F(x, \xi^F, l) \\
\mathcal{K} &= \frac{h^S P^S}{2}\frac{\partial}{\partial x}\tilde{\Gamma}_M^S(x, \xi^S, L) - \frac{h^F P^F}{2}\frac{\partial}{\partial x}\tilde{\Gamma}_M^F(x, \xi^F, l) \\
\mathcal{M} &= -M^S\Gamma_M^S(x, \xi^S, L) + M^F\Gamma_M^F(x, \xi^F, l) \\
\mathcal{N} &= F^S\Gamma_F^S(x\,\xi^S, L) - F^F\Gamma_F^F(x, \xi^F, l) \\
\mathcal{O} &= \frac{h^S P^S}{2}\tilde{\Gamma}_P^S(x, \xi^S, L) + \frac{h^F P^F}{2}\tilde{\Gamma}_P^F(x, \xi^F, l) \\
\mathcal{P} &= \frac{h^S}{2}M^S\tilde{\Gamma}_M^S(x, \xi^S, L) + \frac{h^F}{2}M^F\tilde{\Gamma}_M^F(x, \xi^F, l).
\end{aligned}
\tag{11}
$$

Solution of (8) can be found by numerical integration. The solution interval ($l_1 \le x \le l$) is subdivided into $m$ equal segments with $n$ Gauss integration points in each segment. All *GFA* examples where solved with $m = 50$ and $n = 5$. The integral equations (8) and constraints (3) are then reduced to a system of linear algebraic equations in the form,

$$[S] \begin{Bmatrix} \sigma_z^j \\ \tau_{xz}^j \\ \omega_0 \\ \omega_1 \\ \omega_2 \end{Bmatrix} = \begin{Bmatrix} K_1\{\mathcal{I}_j \mathcal{J}_j \mathcal{K}_j\} + K_2\{\mathcal{L}_j \mathcal{M}_j\} \\ K_3\{\mathcal{N}_j \mathcal{O}_j \mathcal{P}_j\} \\ P^F \\ M^F + P^F \xi^F - F^F \dfrac{h^F}{2} \\ -F^F \end{Bmatrix} \tag{12}$$

where the matrix $S$ is given by,

$$\begin{bmatrix} \delta_{ij} + \alpha_j(K_1\mathcal{A}_{ij} + K_2\mathcal{B}_{ij}) & \alpha_j(K_1\{\mathcal{C}_{ij} + \mathcal{D}_{ij}\} + K_2\mathcal{E}_{ij}) & -K_2 & -K_2 x_j & 0 \\ \alpha_j(K_3\mathcal{F}_{ij}) & \delta_{ij} + \alpha_j(K_3\{\mathcal{G}_{ij} - \mathcal{H}_{ij}\}) & 0 & -K_3\dfrac{h^F}{2} & K_3 \\ \alpha_j & 0 & 0 & 0 & 0 \\ \alpha_j x_j & 0 & 0 & 0 & 0 \\ 0 & \alpha_j & 0 & 0 & 0 \end{bmatrix}. \tag{13}$$

The $\alpha_j$ represent weight factors of Gaussian numerical integration, $\delta_{ij}$ denotes the Kronecker delta and $i, j = 1, \ldots, mn$. The system of linear algebraic equations has dimension ($2mn+3$). The matrix $S$ is neither symmetric nor positive definite, therefore solution of this system of equations is obtained using a direct solver. The system of equations is smaller when compared to FEM analysis, but the procedure still requires a substantial amount of computer time.

In the figures, the stresses evaluated by the Green's function technique will be denoted by $\sigma_{ij}^{GFA}$.

## FINITE ELEMENT ANALYSIS OF THE SKIN–FLANGE ASSEMBLY

To assess the accuracy of the analytical solution, the adhesive layer stresses were also evaluated with a finite element method [6]. A 2D solution was obtained in the *xz*-plane, using the *FEM 2D* code [7]. The mesh consisting of three-node elements was generated using the *T3D* generator [8]. A total of 9081 nodes and 17,428 triangles were used in discretization of

the domain. Six rows of elements were utilized through the thickness of the adhesive layer, except at the leading edges of the bondline, where the mesh was refined to one hundred rows, in an attempt to approximate possible stress singularities. Stress oscillations were detected in small volumes of adhesive and adherend in the proximity of the re-entrant corners and free-edge interfaces at the leading edges of the bondline. To facilitate comparisons of the analytical and finite element results, the layer stresses were averaged through the thickness, in analogy to (8), using the formula,

$$\sigma_{ij}^{\text{average}} = \frac{1}{h^A} \int_0^{h^A} \sigma_{ij}^{\text{element}} dz. \tag{14}$$

In the figures, the stresses evaluated by the finite element method will be denoted by $\sigma_{ij}^{\text{FEM}} \equiv \sigma_{ij}^{\text{average}}$.

### EXAMPLES

Here we illustrate the effect of the proposed prestressing procedure on stress changes in the adhesive layer of the skin–flange assembly shown in Figure 1a, with the selected dimensions listed in Table 1. Table 2 presents selected values of the skin, flange and adhesive elastic moduli. The adhesive properties, were actually measured on the Dexter-Hysol 9339 adhesive [9], and are believed to be typical of other adhesives. Three distinct loading cases were analyzed in the examples, one involving only prestress application and release, one for application of the bending force to the skin, and one for loading of the skin by a tensile force. Table 3 shows the applied load

**Table 1. Dimensions used in numerical examples [mm].**

| L | $l_1$ | $l$ | $l_2$ | $h^F$ | $h^A$ | $h^S$ |
|---|---|---|---|---|---|---|
| 300.0 | 100.0 | 100.0 | 100.0 | 5.0 | 0.5 | 5.0 |

**Table 2. Material properties [MPa].**

| Material | $E(\times 10^3)$ | $G(\times 10^3)$ | $\nu$ |
|---|---|---|---|
| Adherends – Aluminum | 68.9 | 25.9 | 0.33 |
| Adhesive – Dexter-Hysol EA 9339 | 1.78 | 0.65 | 0.37 |

*Table 3. Loading cases [MN/m].*

| | Prestress $P(\times 10^{-3})$ | | Tension Load | Bending Load |
|---|---|---|---|---|
| Loads | before cure | after cure | $F_T(\times 10^{-3})$ | $F_B(\times 10^{-3})$ |
| $P^S(x=L/2)$ | 20.0 | −20.0 | 0.0 | 1.6 |
| $F^S(x=L)$ | 0.0 | 0.0 | 100.0 | 0.0 |
| $P^F(x=l_1, l_1+l)$ | −10.0 | 10.0 | 0.0 | 0.0 |
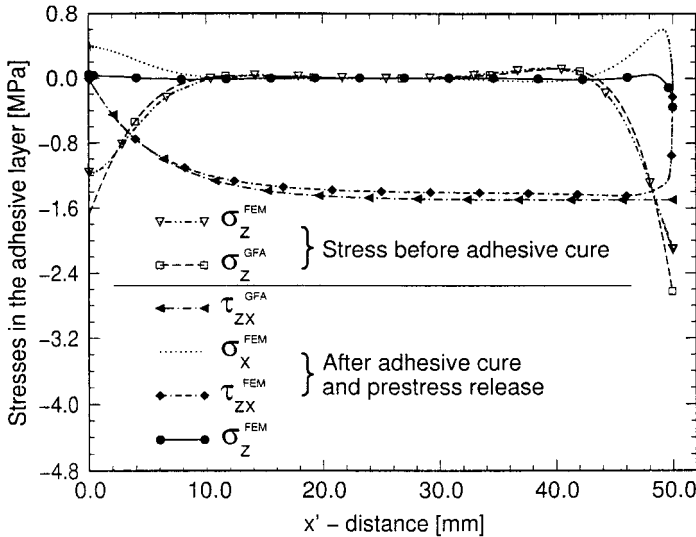


**Figure 4.** *Adhesive layer stresses before and after prestress release, $P = 20 \times 10^{-3}$ MN/m.*

magnitudes $P^S$, $F^S$ and $P^F$ employed in Equations (1), (2), and shown in Figure 1. The remaining forces $M^S$, $M^F$ and $F^F$ are equal to zero. Stress states shown in the figures were obtained by superposition of the residual stress caused by prestress with the stresses caused by the mechanical loading.

Figure 4 presents the stress distribution in the adhesive both before and after cure and prestress release, at the end of the loading sequence shown in Figure 2. Included here is the peel stress $\sigma_z(x)$ that the adhesive supports after cure and under the load shown in Figure 2(a). This stress reaches values of $-1.65$ MPa under the midspan force $P$ at $x' = 0$, and $-2.65$ MPa at the adhesive leading edges at points $D$, but remains close to zero in sections removed from these two locations. Residual thermal stresses that might be caused during cure were not evaluated for lack of required property data. The GFA and FEM methods provide very similar
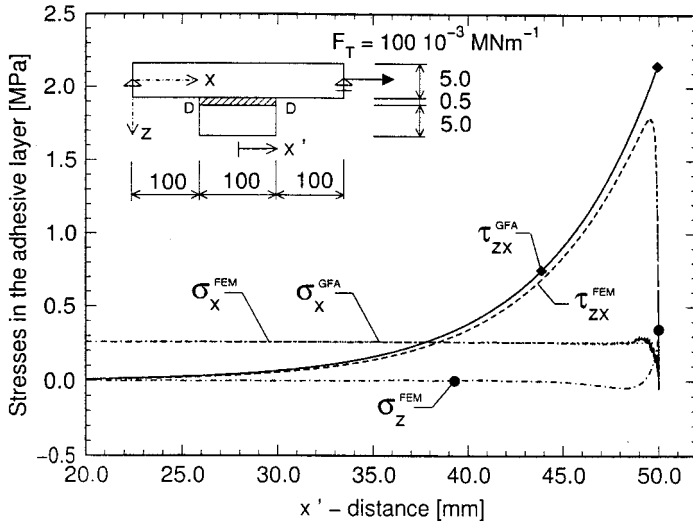
**Figure 5.** *Stresses induced in the adhesive by the tension load $F_T = 100 \times 10^{-3}$ MN/m.*

distributions of the adhesive peel and longitudinal normal stresses before adhesive cure, which agree reasonably well even at the leading edge. However, since the prestress load is removed in the final step of the prestressing procedures, the GFA then evaluates only the residual shear stress in the adhesive, which is in good agreement with the FEM result, except for values at the leading edge. This limitation of the GFA is similar to that displayed by even the more advanced shear lag models [10].

Figure 5 shows the stress distribution caused in the adhesive layer by the tension forces $F_T$ applied to the assembly of Figure 1(a), without any contribution by initial stresses. The peel stress is very low, but the shear stresses reach significant values. Both techniques predict similar distributions of the shear stress in the adhesive at locations away from the outer edges of the flange. The GFA cannot satisfy boundary conditions on the free end of the adhesive, therefore the shear stress prediction at the free ends exceeds that indicated by FEM.

The peel stress concentrations at the leading edges under this type of loading can be approximated only by the FEM, together with the averaging formula, Equation (14). Superimposed stresses caused by prestress and tension loading are shown in Figure 6, and the stress maxima are listed in Table 4. The results demonstrate that the prestress causes a substantial reduction in peel and shear stresses at the leading edge of the bondline. For example, the adhesive shear stress at point $D$ in Figure 1(a) is reduced from 1.79 to 0.56 MPa, or by a factor of 3.19. However, a relatively large
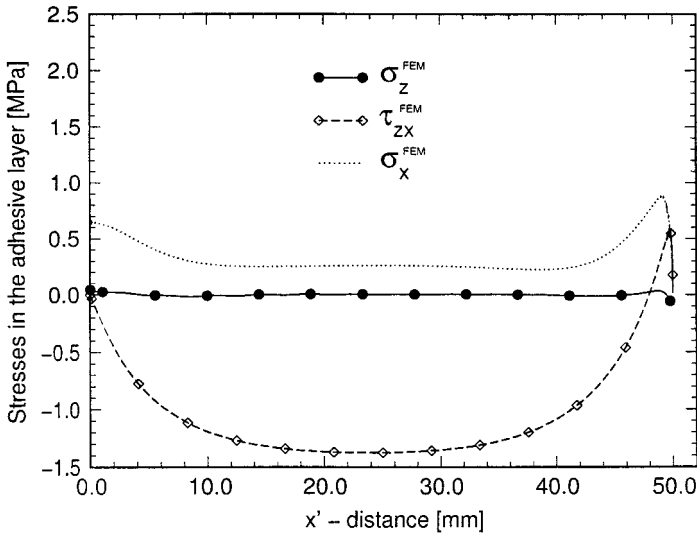
**Figure 6.** Stresses in the adhesive after superposition of prestress and tension loading contributions from Figures 4 and 5.

**Table 4. Adhesive stress maxima caused by tension and bending loads [MPa].**

| Stress | Tension load, $F_T = 100 \times 10^{-3}$ MN/m | | Bending load, $F_B = 1.6 \times 10^{-3}$ MN/m | |
|---|---|---|---|---|
| | without prestress | with prestress | without prestress | with prestress |
| $\sigma_z$ | 0.35 | $-0.06$ | 3.96 | 3.55 |
| $\tau_{zx}$ | 1.79 | 0.56 | 1.92 | 0.77 |
| $\sigma_x$ | 0.29 | 0.87 | 1.22 | 1.46 |

residual shear stress remains in interior sections. The maximum is equal to $-1.38$ MPa, which is lower than the 1.79 MPa value, and it acts in the absence of peel stress, which should make it less likely to cause local decohesion of the bonded interface.

Figure 7 compares adhesive stress distribution predicted by the two methods for the case of bending of the skin–flange assembly by $F_B$. A good agreement between GFA and FEM is found in the peel stress distributions, even in areas of high concentrations. The shear stress is also in very good agreement, except for the zero value at the leading edge, which is restricted by the boundary condition that cannot be satisfied by the GFA. Figure 8 shows the superimposed residual and bending load stress distributions
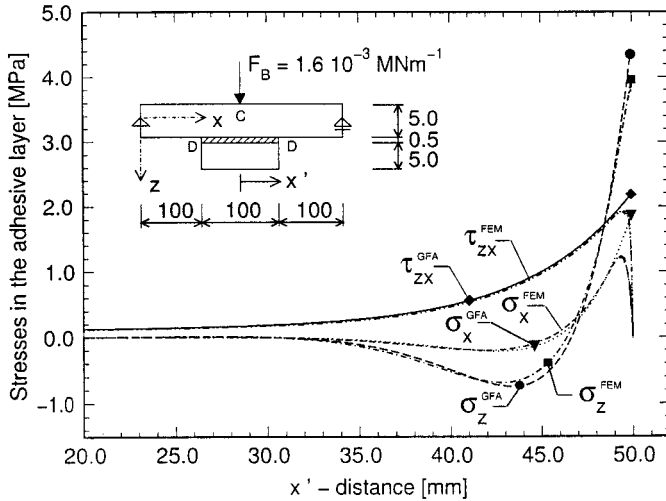
**Figure 7.** *Stresses induced in the adhesive by the bending load* $F_B = 1.6 \times 10^{-3}$ *MN/m.*
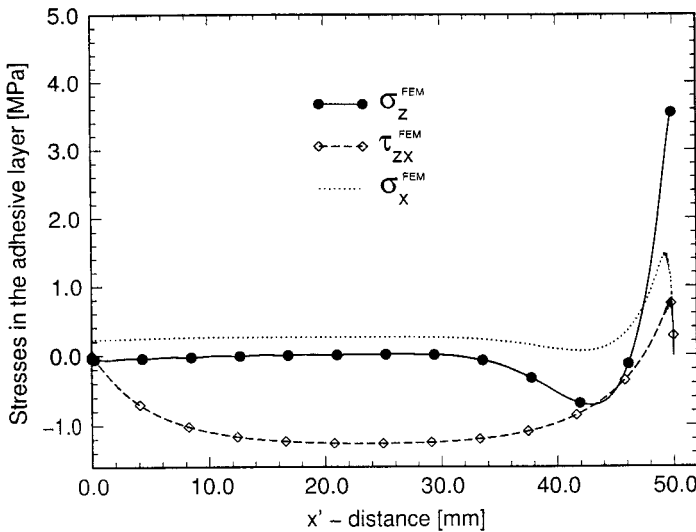


**Figure 8.** *Stresses in the adhesive after superposition of prestress and bending load contributions from Figures 4 and 7.*

obtained from the FEM solutions. Numerical values of the stress maxima can be found in the second part of Table 4.

Figures 9 and 10 present design diagrams that allow determination of the prestress force required for specific reductions of the load-induced stresses at
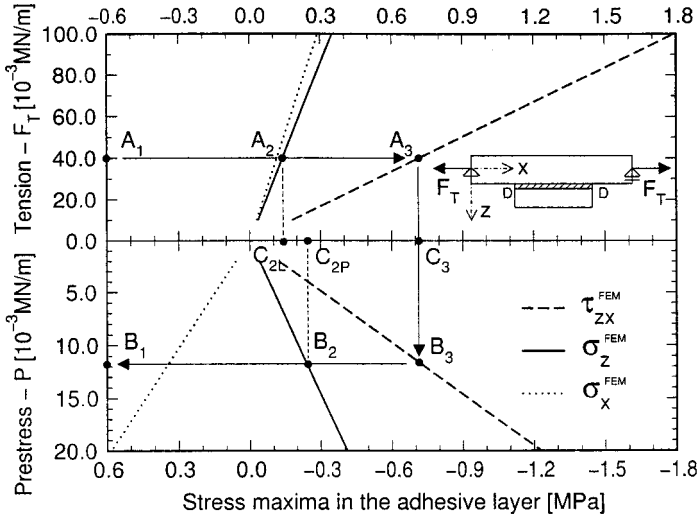
**Figure 9.** Prestress design diagram for the skin/flange assembly subjected to tension.
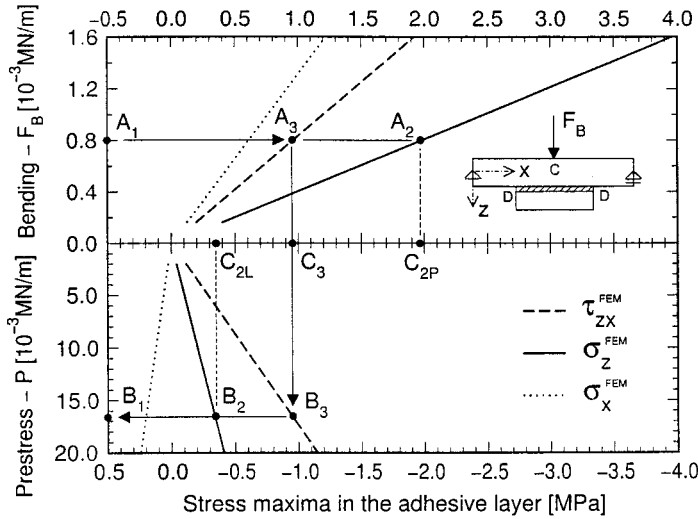


**Figure 10.** Prestress design diagram for the skin/flange assembly subjected to bending.

given load magnitudes. The top parts of these diagrams show straight lines representing scaled maxima of the individual stress components generated by the tension force $F_T$ and bending force $F_B$, respectively. The lines in the bottom parts represent residual stress component maxima generated by

specific magnitudes of the prestress force $P$. For example, for $F_T = 40 \times 10^{-3}$ MN/m, we draw the horizontal line $A_1 \rightarrow A_2 \rightarrow A_3$ to find the respective stress component maxima in the skin–flange structure without prestress. If zero shear stress is desired under the prescribed transverse tension in the prestressed structure, we draw the vertical line $A_3 \rightarrow B_3$, to the intercept with the $\tau_{zx}(x)$ line in the lower half of the figure. Proceeding now horizontally along $B_3 \rightarrow B_2 \rightarrow B_1$, we find the required prestress force $P = 12 \times 10^{-3}$ MN/m. The shear stress in the leading edges of the prestressed structure will now be zero after first application of the selected transverse tension stress. The maximum peel stress is obtained by subtracting the values of $\sigma_z(x)$ at point $C_{2L}$ from that at $C_{2P}$. In the present case, $\sigma_z(C_{2L}) - \sigma_z(C_{2P}) = -0.1$ MPa under tension load.

Figures 11 and 12 show the vertical deflection of the structure along the length of the skin. Zero deflections are imposed at the far ends of the skin. The transverse tension force $F_T = 100 \times 10^{-3}$ MN/m causes the midsection to rise by 0.23 mm. Application of the prestress force $P$ generated a downward deflection of $-0.84$ mm, which is reduced to $-0.61$ mm by the tension force. For the case of bending force of $F_B = 1.6 \times 10^{-3}$ MN/m we obtained the midsection deflection of $-0.5$ mm, and the total midsection deflection of prestressed and loaded beam of $-1.34$ mm. These values confirm that the residual deflection is of the same order of magnitude as that imposed by the load.
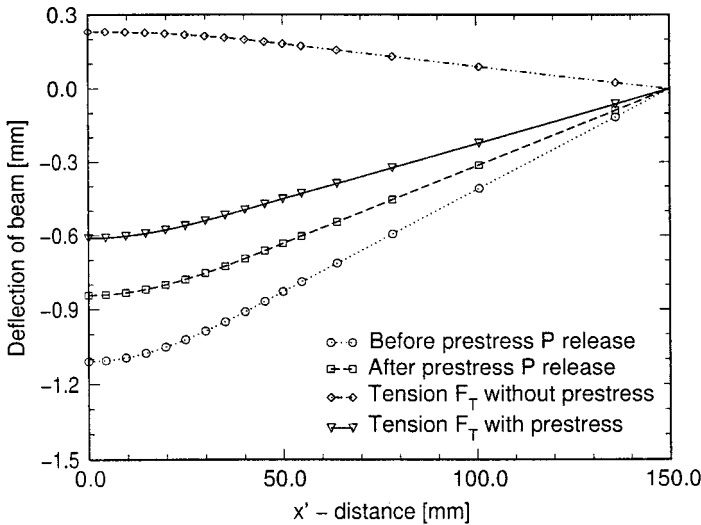


**Figure 11.** *Deflection of the skin/flange assembly, $P = 20 \times 10^{-3}$ MN/m, $F_T = 100 \times 10^{-3}$ MN/m.*
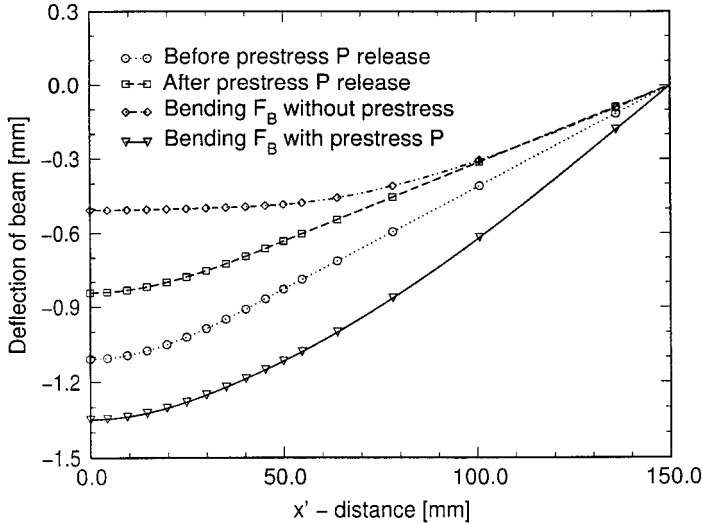
**Figure 12.** Deflection of the skin/flange assembly, $P = 20 \times 10^{-3}$ MN/m, $F_B = 1.6 \times 10^{-3}$ MN/m.

## CLOSURE

The results suggest a relatively simple method of adhesive stresses reduction in a skin–flange assembly loaded either by skin tension and/or bending. While certain special fixtures are required for prestressing, the expected enhancement of load bearing capacity and/or endurance may well be worth the extra cost.

The proposed design diagrams based on elastic stress analysis should suffice and lead to conservative designs in most applications. The more accurate and complete finite element evaluation of the stresses is preferred in construction of the diagrams.

In an actual structure, both flange and skin can be made of a composite laminate consisting of several fibrous layers. Layup details may influence the adhesive stresses at the leading edge of the bondline, and also the interlaminar stresses at the free edges of the laminated flange. Indeed, failure of such joints often originates in the flange end and extends along ply interfaces before reaching the adhesive layer [1–3]. However, inasmuch as the goal was to minimize the stress concentrations at the bondline leading edge by superposition of the prestress and applied loading stress distributions, the differences between the layered and isotropic solutions should not have a large effect on the loading combinations found to generate the minimized stress distributions.

# NOMENCLATURE

$$x, y, z = \text{Cartesian coordinates}$$
$$u, w = \text{displacements in the } x \text{ and } z \text{ directions}$$
$$\varphi_y = \text{rotation about the } y\text{-axis}$$
$$F, P, M = \text{tension force, bending force, bending moment}$$
$$M_y, N_x, Q_z = \text{internal moment, normal and shear forces}$$
$$\sigma_z(x), \tau_{xz}(x), \sigma_x(x) = \text{peel, shear and normal stresses}$$
$$\varepsilon_z(x), \gamma_{xz}(x), \varepsilon_x(x) = \text{peel, shear and normal strains}$$
$$A, I_y = \text{cross section area and moment of inertia}$$
$$L, l = \text{spans of the skin and flange beams}$$
$$\mu, E, G = \text{Poisson's ratio, Young's and shear moduli}$$
$$\kappa = \text{geometric shape correction factor}$$
$$\omega_0, \omega_2, \omega_1 = \text{rigid body deflection, translation and rotation}$$
$$\xi = \text{load position coordinate}$$
$$\tilde{\Gamma}_P(x, \xi, l) = \text{Green's function associated with rotation } \varphi_y \text{ due to force } P$$
$$\tilde{\Gamma}_M(x, \xi, l) = \text{Green's function associated with rotation } \varphi_y \text{ due to moment } M$$
$$\Gamma_P(x, \xi, l) = \text{Green's function associated with deflection } w \text{ due to force } P$$
$$\Gamma_M(x, \xi, l) = \text{Green's function associated with deflection } w \text{ due to moment } M$$
$$\Gamma_F(x, \xi, l) = \text{Green's function associated with translation } u \text{ due to force } F$$

## Superscripts

$$A = \text{adhesive layer}$$
$$S = \text{skin, top beam}$$
$$F = \text{flange, bottom beam}$$

## Subscripts

$$T = \text{tension load}$$
$$B = \text{bending load}$$

# ACKNOWLEDGEMENTS

## APPENDIX

**Green's Functions**

A simply supported beam is considered, loaded by concentrated forces $P$ and $F$, and moment $M$; Figure 13 shows selected coordinate system and also the sign convention adopted for forces and moments acting along the length of the beam. The beam is made of a homogeneous and isotropic material. With reference to Mindlin's kinematic assumptions, the displacement field is selected as,

$$u(x, z) = u_0 + z\varphi_y \quad w(x, z) = w \tag{15}$$

where $u_0$ denotes longitudinal displacement in the $x$-direction, $\varphi_y$ denotes rotation about the $y$-axis and $w$ is the deflection in the $z$-direction. The moment, normal and shear forces then follow from the well-known relations,

$$M_y = EI_y \frac{d\varphi_y}{dx}$$

$$N_x = EA \frac{du_0}{dx}$$

$$Q_z = \kappa GA \left( \varphi_y + \frac{dw}{dx} \right) \tag{16}$$

where $\kappa = 5/6$ is a geometric shape correction factor for a rectangular cross-section.
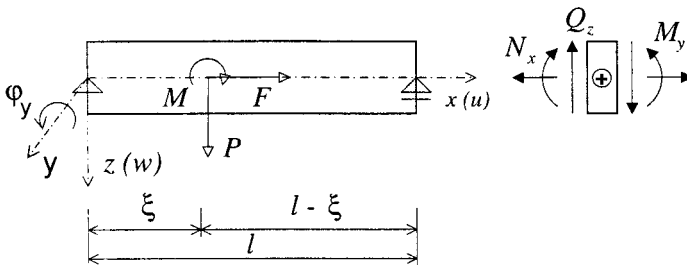


**Figure 13.** Simply supported beam used in derivation of the Green's functions.

With account of work done by shear forces on deformation of beam, the rotation and deflection at any point of the simply supported beam in Figure 13 can be found from standard formulas. The result can be written as,

$$w = P\Gamma_P(x, \xi, l) + M\Gamma_M(x, \xi, l)$$
$$\varphi_y = P\tilde{\Gamma}_P(x, \xi, l) + M\tilde{\Gamma}_M(x, \xi, l) \tag{17}$$

where Green's functions can be reduced to the form,

$$\Gamma_P(x, \xi, l) = \begin{cases} \dfrac{1}{EI_y}\left[\rho\dfrac{l-\xi}{l}x + \dfrac{\xi-l}{l}\dfrac{x^3}{6} - \dfrac{\xi^2 x}{2} + \dfrac{\xi l x}{3} + \dfrac{\xi^3 x}{6l}\right] & 0 \le x \le \xi \\[3mm] \dfrac{1}{EI_y}\left[-\rho\dfrac{\xi x}{l} - \dfrac{\xi x^2}{2} + \dfrac{\xi x^3}{6l} + \dfrac{\xi l x}{3} + \dfrac{\xi^3 x}{6l} + \rho\xi - \dfrac{\xi^3}{6}\right] & \xi \le x \le l \end{cases}$$

$$\tilde{\Gamma}_P(x, \xi, l) = \begin{cases} \dfrac{1}{EI_y}\left[\dfrac{l-\xi}{l}\dfrac{x^2}{2} + \dfrac{\xi^2}{2} - \dfrac{\xi l}{3} - \dfrac{\xi^3}{6l}\right] & 0 \le x \le \xi \\[3mm] \dfrac{1}{EI_y}\left[\xi x - \dfrac{\xi x^2}{2l} - \dfrac{\xi l}{3} - \dfrac{\xi^3}{6l}\right] & \xi \le x \le l \end{cases} \tag{18}$$

and

$$\Gamma_M(x, \xi, l) = \begin{cases} \dfrac{1}{EI_y l}\left[\dfrac{x^3}{6} + \dfrac{l^2 x}{3} + \dfrac{\xi^2 x}{2} - \xi l x\right] & 0 \le x \le \xi \\[3mm] \dfrac{1}{EI_y l}\left[\dfrac{x^3}{6} + \dfrac{l^2 \xi}{3} + \dfrac{\xi^2 x}{2} - \dfrac{l x^2}{2} - \dfrac{l \xi^2}{2}\right] & \xi \le x \le l \end{cases}$$

$$\tilde{\Gamma}_M(x, \xi, l) = \begin{cases} \dfrac{1}{EI_y l}\left[-\dfrac{x^2}{2} + l\xi - \rho - \dfrac{l^2}{3} - \dfrac{\xi^2}{2}\right] & 0 \le x \le \xi \\[3mm] \dfrac{1}{EI_y l}\left[-\dfrac{x^2}{2} + lx - \rho - \dfrac{l^2}{3} - \dfrac{\xi^2}{2}\right] & \xi \le x \le l \end{cases} \tag{19}$$

Here, $E$ is the elastic modulus, $I_y$ is the moment of inertia of the cross-section, $l$ is the span and $\xi$ is the load position coordinate. The parameter $\rho$ is defined as,

$$\rho = \dfrac{EI_y}{\kappa GA} \tag{20}$$

where $G$ is shear modulus and $A$ is cross-sectional area. Similarly, the longitudinal displacement can be written in the form,

$$u_0 = F\Gamma_F(x,\,\xi,\,l) \tag{21}$$

and the corresponding Green's functions are,

$$\Gamma_F(x,\,\xi,\,l) = \begin{cases} \dfrac{1}{EA}[x] & 0 \le x \le \xi \\[2mm] \dfrac{1}{EA}[\xi] & \xi \le x \le l. \end{cases} \tag{22}$$

These equations augment the results (17)–(20), which were also obtained by Gao et al. [4].

## REFERENCES

1. Li, J., O'Brien, T.K. and Rousseau, C.Q. (1997). *Journal of American Helicopter Society*, **42**(4): 350–357.
2. Cvitkovich, M.K., O'Brien, T.K. and Minguet, P.J. (1998). *Composite Materials*: *Fatigue and Fracture* (*ASTM STP 1330*), **7**: 97–121.
3. Krueger, R., Cvitkovich, M.K., O'Brien, T.K. and Minguet, P.J. (2000). *Journal of Composite Materials*, **34**: 1263–1300.
4. Gao, J., Selvarathinam, A.S. and Weitsman, Y.J. (1999). *Journal of Sandwich Structures and Materials*, **1**: 323–339.
5. Gao, J. and Weitsman, Y.J. (2001). *International Journal of Fracture*, **107**: 201–234.
6. Hughes, T.J.R. (1987). *The Finite Element Method*: *Linear Static and Dynamic Finite Element Analysis*. New Jersey, NJ: Prentice-Hall.
7. Matouš, K. (2000). Analysis and optimization of composite materials and structures. Prague, Czech Republic: CTU Reports Vol 4. No. 3/2000.
8. Rypl, D. (1998). Sequential and parallel generation of unstructured 3D meshes. Prague, Czech Republic: CTU Report Vol 2. No. 3/1998.
9. Dvorak, G.J., Zhang, J. and Canyurt, O. (2001). *Composites Science and Technology*, **61**: 1123–1142.
10. Tsai, M.Y., Oplinger, D.W. and Morton, J. (1998). *International Journal of Solids and Structures*, **35**(12): 1163–1185.

## BIOGRAPHIES

### Karel Matouš

Karel Matouš is a postdoctoral research associate at Rensselaer. His research is primarily focused on multiscale numerical modeling of heterogeneous inelastic solids, damage analysis and retardation in two-phase woven composite systems and optimization techniques based on genetic algorithms and their applications. He is a member of ASME, ASCE and ASC.

**George J. Dvorak**

George J. Dvorak is the William Howard Hart Professor of Mechanics at Rensselaer. His research is concerned with modeling of many aspects of mechanical behavior of composite materials and structures. He is a Fellow of AAM, ASME, and SES, and a member of the National Academy of Engineering.